An Estimate of the Effect of 3D Heterogeneous Density Distribution on Coseismic Deformation Using a Spectral Finite-Element Approach

Yoshiyuki Tanaka, Volker Klemann, and Zdeněk Martinec

Abstract

The advancement of the Global Geodetic Observing System (GGOS) has enabled monitoring of mass transport and solid-Earth deformation processes with unprecedented accuracy. Coseismic deformation is modelled as an elastic response of the solid Earth to an internal dislocation. Self-gravitating spherical Earth models can be employed in modelling regional to global scale deformations. Recent seismic tomography and high-pressure/high-temperature experiments have revealed finer-scale lateral heterogeneities in the elasticity and density structures within the Earth, which motivates us to quantify the effects of such finer structures on coseismic deformation. To achieve this, fully numerical approaches including the Finite Element Method (FEM) have often been used. In our previous study, we presented a spectral FEM, combined with an iterative perturbation method, to consider lateral heterogeneities in the bulk and shear moduli for surface loading. The distinct feature of this approach is that the deformation of the entire sphere is modelled in the spectral domain with finite elements dependent only on the radial coordinate. By this, self-gravitation can be treated without special treatments employed when using an ordinary FEM. In this study, we extend the formulation so that it can deal with lateral heterogeneities in density in the case of coseismic deformation. We apply this approach to a longer-wavelength vertical deformation due to a large earthquake. The result shows that the deformation for a laterally heterogeneous density distribution is suppressed mainly where the density is larger, which is consistent with the fact that self-gravitation reduces longer-wavelength deformations for 1-D models. The effect on the vertical displacement is relatively small, but the effect on the gravity change could amount to the same order of magnitude of a given heterogeneity if the horizontal scale of the heterogeneity is large enough.

Keywords

Deformation · Density · Earthquake · Finite element method · Gravity field · Lateral heterogeneity

Y. Tanaka (✉)
Department of Earth and Planetary Science, Graduate School of Science, The University of Tokyo, Tokyo, Japan
e-mail: y-tanaka@eps.s.u-tokyo.ac.jp

V. Klemann
Department 1 Geodesy, German Research Centre for Geosciences, Potsdam, Germany

Z. Martinec
Geophysics Section, Dublin Institute for Advanced Studies DIAS, Dublin 2, Ireland

Faculty of Mathematics and Physics, Charles University, Praha 8, Czech Republic

1   Introduction

Recent advancements in terrestrial and satellite gravity observations have enabled us to monitor mass transports associated with physical processes in the atmosphere, ocean, hydrosphere, and cryosphere with an unprecedent accuracy (Crossley et al. 2013; Wouters et al. 2014). These surface mass transports cause elastic and anelastic deformations of the solid Earth. The resultant deformation of the density interfaces (atmosphere-crust and crust-mantle boundaries, etc.) and compression/dilatation of the solid-Earth material lead to an additional change in the gravity field. By physically modelling this process and comparing the model results, we can learn about deformation mechanisms and rheological properties of the material (e.g., crustal rigidity, mantle viscosity) (Whitehouse 2018).

In addition to surface loading, co- and post-seismic gravity changes induced by large earthquakes have been observed by satellite observations with spatial scales of ∼300 km and amplitudes of several μGals (1 μGal = 10^{-8} m s^{-2}) (e.g., Matsuo and Heki 2011). It is widely accepted that coseismic deformation is physically represented by the elastic response to an internal dislocation. To interpret gravity changes due to large earthquakes, dislocation models have been proposed, which assume a self-gravitating sphere with a 1-D (i.e., spherically symmetric) internal structure (Sun 2014; Zhou et al. 2019). However, seismic tomography and high-temperature/high-pressure experiments nowadays reveal increasingly finer internal structures, particularly in plate subduction zones (Hasegawa and Nakajima 2017). This motivates us to estimate the effects of laterally heterogeneous structures on gravity changes.

So far, several methods have been proposed to calculate coseismic deformation of a laterally heterogeneous Earth model. They can be categorized into two types. (Semi-)analytical perturbation approaches (e.g., Pollitz 2003; Fu and Sun 2008) give a physically clear image on the causes of the deformation. However, the perturbation methods employed make it difficult to deal with strong lateral heterogeneities. On the other hand, fully numerical approaches such as the finite element method (FEM) and the spectral element method can treat such heterogeneities (e.g., Cheng et al. 2019; Pollitz 2020). However, the inclusion of self-gravitation can cause modelling errors when using a commercial package of the FEM. To prevent this, special treatments of self-gravitation are necessary (e.g., Wu 2004; Nield et al. 2022; Vachon et al. 2022).

To address the above difficulties associated with strong heterogeneity and self-gravitation, Tanaka et al. (2019) employed a spectral finite-element approach (Martinec 2000) which combines the advantages of the analytical and numerical approaches. Tanaka et al. (2019) considered lateral heterogeneities in the bulk and shear moduli in modelling of the elastic response to surface loading. This model was applied to ocean tide loading (Huang et al. 2021). However, lateral heterogeneities in density have not yet been considered.

The purpose of this study is to extend the method by Tanaka et al. (2019) for the case of laterally heterogeneous density distributions when modelling coseismic deformation. In Sect. 2, we first explain the way that the spectral finite-element approach facilitates computation of global deformation. Next, we estimate the effect of a 3-D density distribution. In Sect. 3, after some checks of the method, we demonstrate the effects of 3-D density distribution on the coseismic vertical displacement and gravity change due to a megathrust earthquake. Finally, in Sect. 4, results and future work are summarized.

2   Method

2.1   An Overview of the Spectral Finite-Element Approach

We apply the approach to the governing equations for the elastic deformation of a self-gravitating sphere (Farrell 1972) under free-surface and internal source conditions represented by double-couple forces that are equivalent to a dislocation. No terms are ignored/approximated in the governing equations and no additional forces/boundary conditions are added. The governing equations are converted into a corresponding variational problem associated with the elastic strain and gravitational energies ($E \equiv E_{\text{bulk}} + E_{\text{shear}} + E_{\text{grav}}$) and the work derived from the surface and source conditions (δF) (Tanaka et al. 2014):

$$\delta E (\boldsymbol{u}, \delta\boldsymbol{u}, \phi_1, \delta\phi_1) = \delta F (\delta\boldsymbol{u}, \delta\phi_1), \qquad (1)$$

where $\boldsymbol{u}$, ϕ_1 and δ denote the displacement, the incremental gravity potential and the variation, respectively. The variation in the shear strain energy is given as

$$\delta E_{\text{shear}} (\boldsymbol{u}, \delta\boldsymbol{u}) \equiv \int_V 2\mu (\boldsymbol{\epsilon} \cdot \delta\boldsymbol{\epsilon}) \, dV, \qquad (2)$$

where μ and $\boldsymbol{\epsilon}$ denote the shear modulus and the strain tensor, respectively, and V indicates a volume integral over the entire sphere. The source time function included in δF is assumed to be a step function. The solution of Eq. (1) gives the static deformation which balances the double-couple forces.

Commercial FEM packages usually employ 3-D finite elements to compute Eqs. (1) and (2). In our approach, however, Eq. (2) is decomposed into the 1-D and residual

3-D parts:

$$\delta E_{\text{shear}} = \int_V 2\mu_0(r)\,(\boldsymbol{\epsilon}\cdot\delta\boldsymbol{\epsilon})\,dV$$
$$+ \int_V 2\Delta\mu\,(r,\theta,\varphi)\,(\boldsymbol{\epsilon}\cdot\delta\boldsymbol{\epsilon})\,dV, \tag{3}$$

where (r, θ, φ) denote the radial distance, colatitude and longitude, respectively, and μ_0 and $\Delta\mu$ represent the shear modulus of the reference 1-D model and the difference from μ_0, respectively. We apply 1-D finite elements in the radial direction and represent angular dependencies of the strain field by tensor spherical harmonics. Then, thanks to their orthogonal properties, the first term on the LHS of Eq. (3) becomes straightforward for numerical evaluation. The second term is numerically evaluated (Martinec 2000). We assume that lateral heterogeneities exist only within a small volume ΔV near the source (i.e., $\Delta\mu = 0$ outside ΔV and $\Delta V \ll V$). Then, we can take the integration domain of the second term to be much smaller than the entire sphere. These treatments reduce costs for computing the global deformation to a large extent.

2.2 Inclusion of Laterally Heterogeneous Density Distributions

The variation in the gravitational energy for the 1-D case is given by Eq. (42) of Martinec (2000) as

$$\delta E_{\text{grav}}\big(\boldsymbol{u}, \phi_1, \delta\boldsymbol{u}, \delta\phi_1\big)$$
$$\equiv \int_V \rho_0\big[\,\text{grad}\,(\boldsymbol{u}\cdot\text{grad}\,\phi_0)\big]$$
$$- \text{div}\,\boldsymbol{u}\,\text{grad}\,\phi_0 + \text{grad}\,\phi_1\big]\cdot\delta\boldsymbol{u}\,dV$$
$$+ \int_V \Big[\frac{1}{4\pi G}\big(\text{grad}\,\phi_1\cdot\text{grad}\,\delta\phi_1\big) + \rho_0\big(\boldsymbol{u}\cdot\text{grad}\,\delta\phi_1\big)\Big]dV, \tag{4}$$

where G is the gravitational constant and $\rho_0(r)$ and $\boldsymbol{g}_0(r) \equiv \text{grad}\,\phi_0$ denote the density and gravity for the initial state before deformation takes place. In the following, we extend this energy variation to the laterally heterogeneous case and will come back to the remaining 3-D part of the energy variation which is not included in Eq. (4).

When there is a small lateral heterogeneity, the initial stress field, before an earthquake occurs, deviates only slightly from the hydrostatic state. In the following, $\boldsymbol{u}$ and ϕ_1 represent the coseismic deformation with respect to this laterally heterogeneous initial state. We substitute $\rho_0 + \Delta\rho(r,\theta,\varphi)$ and $\boldsymbol{g}_0 + \Delta\boldsymbol{g}(r,\theta,\varphi)$ into ρ_0 and $\boldsymbol{g}_0$ in Eq. (4), respectively. Here, $\Delta\rho$ denotes the difference from the 1-D density distribution at the initial state due to a given lateral heterogeneity. Since gravity is linearly dependent on density, Poisson's equation is valid for the incremental density. Therefore, div grad $\Delta\phi = 4\pi G\Delta\rho$ holds and $\Delta\boldsymbol{g}$ ($\equiv$ grad $\Delta\phi$) denotes the static gravity increment due to $\Delta\rho$. Subtracting the energy variation for the 1-D case from the result, neglecting the terms including the product of $\Delta\rho\Delta g$, and considering the orthogonality of vector spherical harmonics, we obtain

$$\delta E^{\Delta}_{\text{grav},jm} = \delta E^I_{\text{grav},jm}\,(\Delta\rho) + \delta E^{II}_{\text{grav},jm}\,(\Delta g), \tag{5}$$

where

$$\delta E^I_{\text{grav},jm} = \sum_{j'm'}\int_{\Delta V} \Delta\rho\,(r,\theta,\varphi)$$
$$\left[\begin{array}{l}\left(-\dfrac{4g_0 U_{jm}}{r} + \dfrac{Jg_0 V_{jm}}{r} + \dfrac{dF_{jm}}{dr} + 8\pi G\rho_0 U_{jm}\right)\delta U^*_{j'm'} \\ + \left(\dfrac{g_0 U_{jm}}{r} + \dfrac{F_{jm}}{r}\right)\delta V^*_{j'm'} + \left(U_{jm}\dfrac{d\delta F^*_{j'm'}}{dr} + \dfrac{V_{jm}}{r}\delta F^*_{j'm'}\right)\end{array}\right]dV \tag{6}$$

and

$$\delta E^{II}_{\text{grav},jm}$$
$$= \sum_{j'm'}\int_V \Delta g\,(r,\theta,\varphi)\,\rho_0(r)$$
$$\left[\left(-\dfrac{4U_{jm}}{r} + \dfrac{JV_{jm}}{r}\right)\delta U^*_{j'm'} + \left(\dfrac{U_{jm}}{r}\right)\delta V^*_{j'm'}\right]dV \tag{7}$$

(c.f., Eq. (65) of Martinec (2000)). Here, $(U(r), V(r), F(r))_{jm}$ denote spherical harmonic coefficients for the vertical and horizontal displacements and the incremental gravity potential at degree j, order m. The asterisks represent complex conjugates and $J = j(j + 1)$ is a factor originating from div $\boldsymbol{u}$, and Δg represents the magnitude of $\Delta\boldsymbol{g}$ in the radial direction. The products of the vector spherical harmonics in the integrands (e.g., $\mathbf{S}^{(-1)}_{jm}\cdot\mathbf{S}^{(-1)}_{j'm'}$)(see, Eq. (B1) of Martinec (2000)) are omitted for simplicity. Note that, in the 3-D case, summations over j' and m' appear, indicating a modal coupling with other degrees and orders.

The integrands in Eqs. (6) and (7) have a common term

$$\left(-\dfrac{4U_{jm}}{r} + \dfrac{JV_{jm}}{r}\right)\delta U^*_{j'm'} + \left(\dfrac{U_{jm}}{r}\right)\delta V^*_{j'm'}$$
$$\equiv K_U(r)\delta U^*_{j'm'} + K_V(r)\delta V^*_{j'm'}. \tag{8}$$

By this notation, the corresponding energy variations for j', m' can be written as

$$\delta E^{I'}_{\text{grav},jm} \equiv \int_{\Delta V} \Delta\rho\,(r,\theta,\varphi)\,g_0\left[K_U\delta U^*_{j'm'} + K_V\delta V^*_{j'm'}\right]dV \tag{9}$$

and

$$\delta E_{\text{grav},jm}^{II'} \equiv \int_V \rho_0(r)\Delta g\,(r,\theta,\varphi)\Big[K_U\delta U_{j'm'}^* + K_V\delta V_{j'm'}^*\Big]dV. \tag{10}$$

It is expected that $\left|\delta E_{\text{grav},jm}^{I'}\right| \gg \left|\delta E_{\text{grav},jm}^{II'}\right|$ for two reasons. First, $\Delta\rho/\rho_0$ is $\sim 10^{-2}$ and $\Delta g/g_0$ is $\sim 10^{-5}$ (10 mGal/980 Gal) in the real Earth, which means $\Delta\rho g_0 \gg \rho_0\Delta g$. Second, Δg and $K_{U,V}$ are smaller outside ΔV in Eq. (10) (note that the source is located within ΔV and the deformation (i.e., U_{jm} and V_{jm} included in $K_{U,V}$) decays with the square of the epicentral distance (Okada 1992). Assuming that ΔV has a shape of a spherical cap, we will roughly estimate a ratio between the magnitudes of Eqs. (9) and (10). We assume that $K_U \sim K_V \sim D/r$, where $D = 1$ within ΔV and $D = d_s/(a-r)^2$ outside ΔV. Here, d_s (=40 km) and a (=6,371 km) are the depth of the point source and the Earth's radius. The density of the 1-D case, ρ_0, is homogeneous within the Earth and $\Delta\rho$ is set to $\frac{1}{100}\rho_0$ within ΔV. The integration is performed by an elementary numerical difference method. The result is shown in Sect. 3.1.

Now, we come back to the part which is excluded in the energy variation in Eq. (4). In the 3-D case, the last three terms in Eq. (A7) of Martinec (2000) add to Eq. (4). The last term of Eq. (A7) associated with discontinuities within the Earth vanishes in the present case because we do not consider lateral heterogeneities near the core-mantle boundary (CMB) and the normal vector of the fault is orthogonal to the displacement (shear slip is assumed). The third term in Eq. (A7) associated with the surface integral vanishes when ΔV and the deformation field caused by the source are line symmetric, as employed in Sect. 2.4. The second term in Eq. (A7) is given as

$$\tfrac{1}{2}\int_V \Big[(\text{grad }\rho_0\cdot\delta\boldsymbol{u})\,(\boldsymbol{u}\cdot\text{grad }\phi_0) - (\text{grad }\rho_0\cdot\boldsymbol{u})\,(\delta\boldsymbol{u}\cdot\text{grad }\phi_0)\Big]dV. \tag{11}$$

Substituting $\rho_0 + \Delta\rho(r,\theta,\varphi)$ and $\boldsymbol{g}_0 + \Delta\boldsymbol{g}(r,\theta,\varphi)$ into Eq. (11), and based on the same argument as for Eq. (10), we can approximate Eq. (11) as

$$\frac{g_0}{2}\int_{\Delta V}\big[(\text{grad }\Delta\rho\cdot\delta\boldsymbol{u})\,U - (\text{grad }\Delta\rho\cdot\boldsymbol{u})\,\delta U\big]dV. \tag{12}$$

We consider the case where $\Delta\rho$ is constant within ΔV. Then, $\text{grad}\Delta\rho$ takes non-zero values only on the boundary of ΔV. Furthermore, we note that the terms including the vertical gradient of the density in Eq. (12) cancel out on a horizontal surface. Therefore, we consider only the vertical surface which consists of the boundary of ΔV. We derive a weak formulation and evaluate the magnitude of Eq. (12). The result is shown in Sect. 3.1.

2.3 Iteration

The effect of the lateral heterogeneity is finally determined by solving the following equation iteratively, as described in Tanaka et al. (2019).

$$\begin{aligned}\delta E_{\text{1D}}\left(\boldsymbol{u}^i,\delta\boldsymbol{u},\phi_1^i,\delta\phi_1\right) \\= \delta F\left(\delta\boldsymbol{u},\delta\phi_1\right) - \delta E_{\text{grav}}^{\Delta}\left(\boldsymbol{u}^{i-1},\delta\boldsymbol{u},\phi_1^{i-1},\delta\phi_1\right),\end{aligned} \tag{13}$$

where δE_{1D} denotes the energy variation excluding the effects of lateral heterogeneities. At the first step ($i=1$), $\delta E_{\text{grav}}^{\Delta}$ is set to zero. For $i \geq 2$, $\delta E_{\text{grav}}^{\Delta}$ is computed with the solution obtained at the previous step. This iteration is repeated until $(\boldsymbol{u},\phi_1)^i \cong (\boldsymbol{u},\phi_1)^{i-1}$. The convergence behavior is shown in Sect. 3.1.

2.4 Model Setting

We use a synthetic rectangular fault model to simulate coseismic deformation due to a megathrust earthquake. The length and width of the fault are 550 km and 100 km, respectively, and a slip of 10 m is uniform on the fault ($M_W = 8.7$). The strike, dip and rake angles are ($0°$, $25°$, $90°$) and the fault is dipping to the west (Fig. 1). The fault is distributed within $-2.5° \leq \beta \leq 2.5°$ and $104.1° \leq \varphi \leq 105°$, where β and φ denote latitude and longitude, respectively, and the fault is located at depths ranging from 15 km to 57 km.

PREM (Dziewonski and Anderson 1981) is considered as the reference Earth model. In Model A, we assume that the density is larger by 5% than in the reference model within a region of $-20° \leq \beta \leq 20°$, $80° \leq \varphi \leq 110°$ and depths from 0 to 670 km, including the above fault (Fig. 1). In Model B, the heterogeneity of Model A is given in a region excluding the fault ($80° \leq \varphi \leq 104°$). The elastic parameters in Models A and B are the same as in PREM. The results shown below are proportional to the magnitude of the heterogeneity. If the
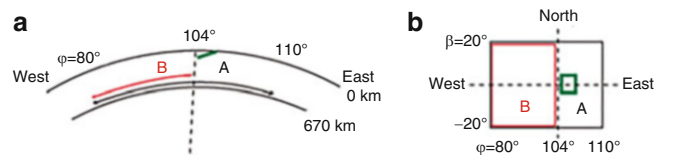
Fig. 1 The fault and Earth structure models used in the computation. (a) A cross section of the Earth model at latitude $\beta = 0$. The rectangular reverse fault (green line) consists of 92 point sources having the same dip-slip mechanism. The density in the upper mantle is increased by 5% with respect to the PREM for the longitudinal ranges (φ) shown by the black (Model A) and red (Model B) arrows. (b) A top view. The green box shows a vertical projection of the fault. The horizontal ranges where the density is increased are shown by the black (Model A) and red (Model B) boxes

lateral heterogeneity is 1% instead of 5%, then, the effect on the deformation becomes 1/5 the magnitude of the case shown here

Assuming a future satellite gravity mission, we set the cut-off spherical harmonic degree as 100 and applied no spatial filter such as a Gaussian filter to the computational results. The radial intervals of the finite elements, $\triangle r$, depend on depth and are set as follows: $\triangle r = 1$ km for depths 0–100 km, 5 km for 100–150 km, 10 km for 150–300 km, 15 km from 300 km to the CMB and 20 km below the CMB. The horizontal grid needed for numerical computations of the 3-D part is set according to the method described in Martinec (2000). The numbers of the grid points are 152 and 512 in latitude and longitude, respectively.

The effects of lateral heterogeneities of Models A and B are evaluated as the differences with respect to the reference model. The results are shown in Sects. 3.2–3.3.

3   Results and Discussions

3.1   Check of the Approximations Used

Table 1 shows the ratio $\left| \delta E_{grav,jm}^{II'} \right| / \left| \delta E_{grav,jm}^{I'} \right|$ for density distributions with different radii and thicknesses. The ratios are less than 0.5% for all the cases. The reason why the result for depths 0–670 km is equal to that for depths 0–100 km is that the deformation is concentrated in the proximity of the source, which is located at the depth of 40 km, and the integrand in $\delta E_{grav,jm}^{II'}$ below the depth of 100 km is much smaller than in $\triangle V$. These results allow us to neglect $\delta E_{grav,jm}^{II}$ (Eq. 7) for practical applications because the effects of lateral heterogeneities in the density are at most a few percent of the peak coseismic deformation as shown later, and hence neglecting $\delta E_{grav,jm}^{II}$ causes an error of the order of only 0.01%, which is below detectable levels of geodetic observations.

Next, we compare the surface deformation for Model B obtained by including and excluding the energy variation represented by Eq. (12). The results show that, when the energy variation of Eq. (12) is included, the vertical displacement and the gravity change decrease by 0.4 mm and 0.04 μGal at the most, where the density distribution laterally changes near the west side of the fault ($\varphi \sim 104°$). The magnitudes of these decreases are less than 0.1%, if compared with the deformation at the corresponding location in the 1-D case (peak p_2 in Figs. 2a and 3a). However, for the vertical displacement, a difference of 0.4 mm is not negligible because the effect of the lateral heterogeneity is of the same order of magnitude. Figure 2b, c show that the differences between the cases including and excluding the

Table 1 The ratio of the gravitational energies $\left| \delta E_{grav,jm}^{II'} \right| / \left| \delta E_{grav,jm}^{I'} \right|$ estimated for different density distributions. The density is increased by 1% within a cap-like volume occupying $0 \le \theta \le \alpha$, $0 \le \varphi \le 2\pi$ and the depths shown below (θ and φ denote colatitude and longitude, respectively). A point source is located 40 km below the north pole (i.e., $\theta = 0$)

| α	Depth	II/I
(deg)	(km)	(%)
10	0–30	0.28
20	0–100	0.43
20	0–670	0.43
30	0–100	0.45
45	0–100	0.48

energy variation are visible. For the gravity change, the effect of lateral heterogeneity is of the order of μGal. Therefore, a difference of 0.04 μGal amounts to only ~1% of the effect of lateral heterogeneity. In the subsequent sections, we discuss results obtained by including the energy variation of Eq. (12).

Table 2 shows the result of iterations for Model B. We see that the difference is largest between $i = 1$ and 2, amounting to 0.03–0.3%. After $i = 2$, the differences are smaller than 0.02%, indicating that the spherical harmonic coefficients for the vertical displacement converged at 10^{-4} level. A similar tendency is seen for Model A.

These results are summarized as follows. As far as a relatively large-scale heterogeneity like Models A and B is concerned, the energy variation arising from $\triangle g$ (Eq. 7) is negligible and the energy variation represented by Eq. (12) is not, in estimating the effect due to the lateral heterogeneity on the coseismic deformation. A few steps of iteration are sufficient.

3.2   Vertical Displacement

Figure 2a shows the vertical displacement along the latitude line passing through the center of the fault ($\beta = 0°$ and $80° \le \varphi \le 130°$) computed for the reference model. We see an uplift of ~1 m at $\varphi \sim 105°$ above the shallower edge of the fault (p_1) and a subsidence of 0.5 m at $\varphi \sim 102°$ above the deeper edge of the fault (p_2), which is a well-known pattern observed for thrust-type fault motion. The blue curve in Fig. 2c shows the difference between model A relative to the reference model. We see that the pattern is roughly opposite to that in Fig. 2a (compare p_1 with p_3 and p_2 with p_4), but the effect is very small. The largest lower peak (p_3) has amplitude of 1 mm, indicating that a 5% increase in density reduces the coseismic maximum uplift seen at p_1 by ~0.1%.
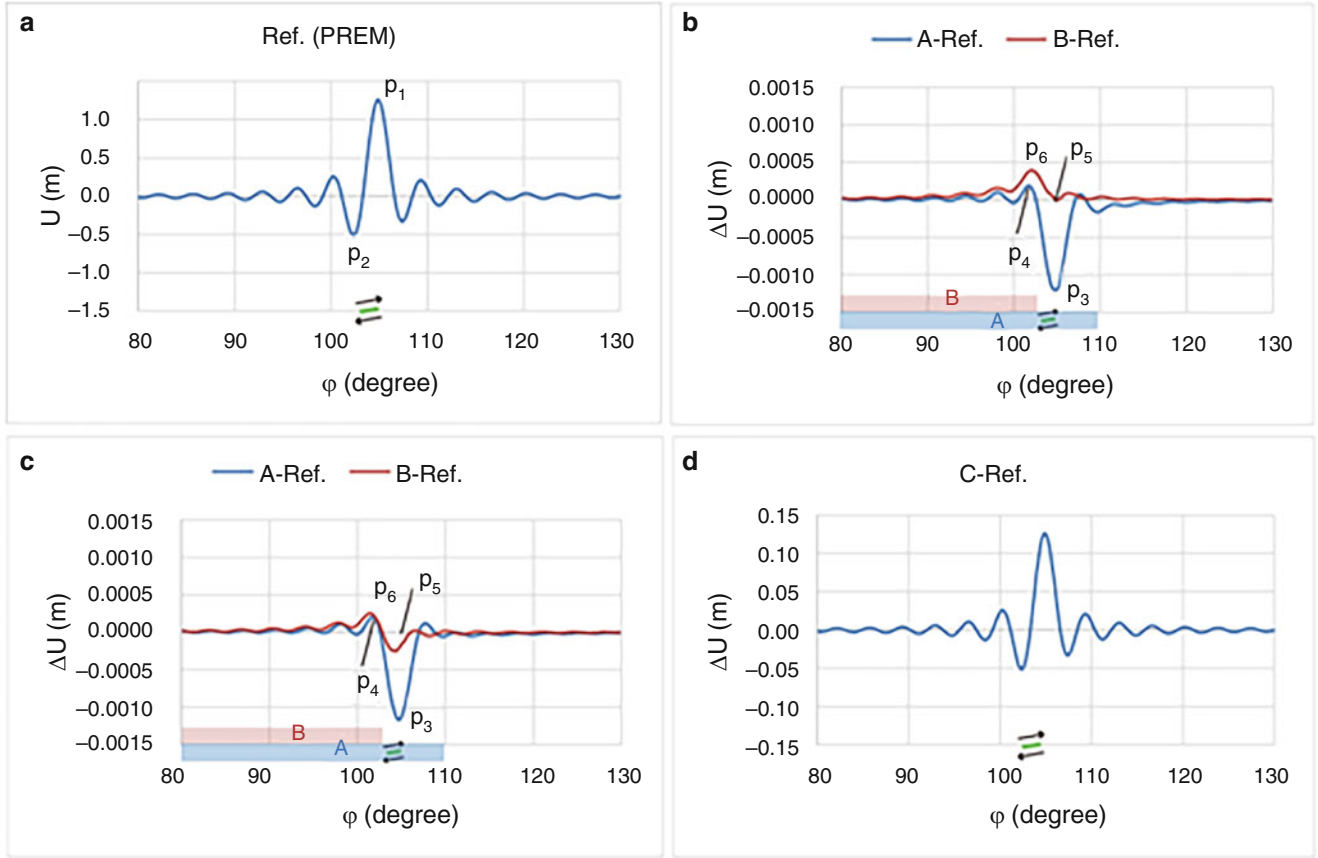
Fig. 2 Coseismic vertical displacements at latitude $\beta = 0$ for different Earth models. The horizontal axes denote longitude (Fig. 1). The green line denotes the fault, and the cut-off spherical harmonic degree is 100. (**a**) The vertical displacement, U, for the reference 1-D model (PREM). (**b**) The difference in the vertical displacements computed for the reference model and Model A (blue)/B (red). The energy variation of Eq. (12) is excluded. The blue and red boxes denote the ranges where the density in the upper mantle is increased. (**c**) The same as in (**b**) but Eq. (12) is included. (**d**) The same as in (**c**) but the shear modulus in the upper mantle is increased instead of the density (Model C)
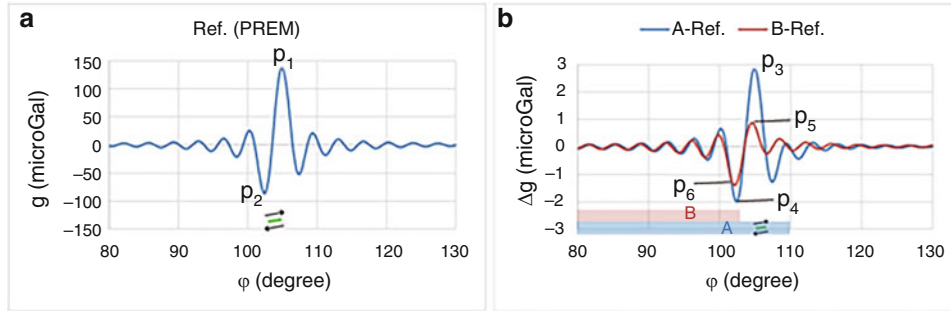
Fig. 3 The same as in Fig. 2, but the coseismic gravity change is shown. (**a**) The gravity change, g', for the reference 1-D model. (**b**) The difference in the gravity changes computed for the reference model and Model A (blue)/B (red). Note that the patterns are opposite to those in the vertical displacements in Fig. 2 (**b**) and that the relative magnitude amounts to a few percent (compare peaks p_1 and p_3 or p_2 and p_6)

The reduction of the vertical displacement is consistent with the fact that the inclusion of self-gravitation suppresses longer-wavelength deformations for a flat-Earth model (Barbot and Fialko 2010). This can be understood if we consider that an increase in density enhances the gravitational effect (i.e., $\rho_0 g_0$ is replaced by $(\rho_0 + \triangle\rho)g_0$ where $\triangle\rho > 0$).

For comparison, Fig. 2d shows a result when the shear modulus is increased by $\sim$10% for the same region as the region where the heterogeneity is considered in Model A. We see that the pattern of the difference is the same as in the coseismic change and that amplitude increases by $\sim$10%. This indicates that the difference in the vertical displacement is proportional to the difference in the shear modulus. This

Table 2 A convergence of the solution for Model B. The first column (i) shows numbers of iterations (Sect. 2.3). U_{jm} denote the real part of the spherical harmonic coefficient of the vertical displacement at the surface ($r = a$) for degree j and order m

i	$U_{10,0}$	$U_{20,10}$	$U_{60,40}$	$U_{100,100}$
1	−8.589E-4	−7.490E-4	−2.584E-4	3.055E-3
2	−8.617E-4	−7.496E-4	−2.585E-4	3.054E-3
3	−8.617E-4	−7.496E-4	−2.585E-4	3.054E-3
4	−8.617E-4	−7.496E-4	−2.585E-4	3.054E-3

is because the energy of the seismic source is proportional to the shear modulus. In contrast, the effect of the density is only ∼1/20 of the given heterogeneity in magnitude (namely, the 5% increase in the density caused the 0.1% increases in the vertical displacement).

Next, we compare Models A and B. The red curve in Fig. 2c shows the result for Model B. We see that, when the heterogeneity is excluded from the source region, the largest negative peak at $\varphi \sim 105°$ for Model A (p_3) is reduced (p_5) and that Model B shows a close pattern to Model A on $\varphi < 104°$. This indicates that the reduction of the vertical displacement occurs mainly in the region where the density is increased.

3.3 Gravity Change

We have seen that the effect of the laterally heterogeneous density distribution on the vertical displacement is as small as 0.1% of the coseismic change. However, the effect on the gravity change is an order of magnitude larger, as will be shown below.

Figure 3a shows the coseismic gravity change computed for the reference model. The pattern resembles the vertical displacement in Fig. 2a. The blue curve in Fig. 3b shows the difference between Model A and the reference model. We see that the pattern is similar to the coseismic change in Fig. 3a and that the increase in amplitude amounts to ∼2% of the coseismic gravity change (compare p_1 with p_3).

The reason why the effect on the gravity change is larger than on the vertical displacement can be explained by a Bouguer (slab) approximation:

$$\left(g' + \Delta g' \right)\big|_{r=a} \sim 2\pi G \left(\rho_0 + \Delta \rho \right)\big|_{r\sim a} \left(U + \Delta U \right)$$
$$\cong 2\pi G \left(\rho_0 U + \rho_0 \Delta U + U \Delta \rho \right)\big|_{r\sim a}. \quad (14)$$

In this equation, a denotes the Earth's radius, and g' and U are the surface gravity change and the vertical displacement caused by the deformation for the reference model. $\triangle$ means the difference from the reference model due to the inclusion of the lateral heterogeneity. The first term in the rightmost side of Eq. (14) represents the gravity change due to the

deformation in the 1-D case. In the second term, $\triangle U$ is opposite to U and is significantly smaller than U (Sect. 3.2). So, the last term is dominant as the effect of the lateral heterogeneity, indicating that the deformation for the 1-D model and the local density distribution take effects and that the ratio of the third term to the first term is $\triangle \rho / \rho_0$.

The red curve in Fig. 3b shows the result for model B. We see that the difference between Models A and B is small on $\varphi \leq 104°$ where the heterogeneity in Model B is present and that amplitudes of Model B become smaller for $\varphi > 104°$. This result suggests that the effect of the lateral heterogeneity on the gravity change is larger where the heterogeneity is present, as seen for the vertical displacement.

Fu and Sun (2008) estimated coseismic gravity changes for a 3-D heterogeneous spherical Earth model. The magnitude of the lateral heterogeneity in the density used in their computation was ∼±0.5% with respect to the PREM. In the shallow upper mantle, the main sources of heterogeneity are subducting slabs. Their result shows that the effect of lateral heterogeneity on the gravity change caused by a point dislocation placed at 100 km or below was 0.01–0.03%. In our result, the effect on the gravity change is of the same order of magnitude as for the heterogeneity. That means that, if a heterogeneity was 0.5%, the effect on the gravity change would be ∼0.5% in our model. A few reasons are considered to explain why our result is an order of magnitude larger than their result; In our study, (1) the horizontal scale of the heterogeneity given is much larger than the thickness of slab, (2) the source depth is shallower than 100 km, (3) the cut-off degree is lower and thus longer-wavelength deformations are dominant, which are more strongly affected by the gravity field (generated by the initial static density distribution). To examine the effect due to a fine 3-D density structure for a shallow seismic source, higher-degree terms must be computed, which will be done in a next study.

4 Conclusions

We developed a spectral finite-element approach for estimating the effects of laterally heterogeneous density distributions on coseismic deformations. Considering that deformations due to a great earthquake will be observed by a future satellite gravity mission, we computed a coseismic vertical displacement and gravity change up to $j_{max} = 100$ for Earth models with a large-scale lateral heterogeneity being present near the seismic fault. The results show that the increase in the density within the upper mantle by 5% over a horizontal scale of ∼3,000 km could suppress the vertical displacement by an order of 0.1% and amplify the gravity change by an order of 1% with respect to the case for the reference 1-D model. The differences from the 1-D model were larger where the heterogeneity was present, and a larger increase in

the gravity change than in the vertical displacement occurs, because the local density structure maps directly into the gravity change.

In this study, we imposed a few limitations on the heterogeneity: a large horizontal scale, being present in the vicinity of the source, and simple (symmetric) geometry. Under these conditions, we showed that the estimation of the energy variation of Eq. (A7) of Martinec (2000) could be simplified. For more complex density distributions by subducting slabs, plumes, surface topography and bathymetry, it might be more effective to directly compute the energy variation of Eq. (A2), which is an alternative representation of Eq. (A7). Furthermore, for surface loading, gravity increments due to lateral heterogeneities in the density enter into the boundary conditions. In this case, it should be examined whether neglecting the second term of the gravitational energy (Sect. 2.2) is valid. To extend the applicability of the spectral FEM to more general cases is a future challenge.

References

Barbot S, Fialko Y (2010) A unified continuum representation of post-seismic relaxation mechanisms: semi-analytic models of afterslip, poroelastic rebound and viscoelastic flow. Geophys J Int 182:1124–1140. https://doi.org/10.1111/j.1365-246X.2010.04678.x

Cheng H, Zhang B, Huang L, Zhang H, Shi Y (2019) Calculating coseismic deformation and stress changes in a heterogeneous ellipsoid earth model. Geophys J Int 216:851–858. https://doi.org/10.1093/gji/ggy444

Crossley D, Hinderer J, Riccardi U (2013) The measurement of surface gravity. Rep Prog Phys 76:046101. https://doi.org/10.1088/0034-4885/76/4/046101

Dziewonski AM, Anderson A (1981) Preliminary reference earth model. Phys Earth Planet Inter 25:297–356

Farrell WE (1972) Deformation of the earth by surface loads. Rev Geophys Space Phys 10:761–797

Fu G, Sun W (2008) Surface coseismic gravity changes caused by dislocations in a 3-D heterogeneous earth. Geophys J Int 172:479–503. https://doi.org/10.1111/j.1365-246X.2007.03684.x

Hasegawa A, Nakajima J (2017) Seismic imaging of slab metamorphism and genesis of intermediate-depth intraslab earthquakes. Prog Earth Planet Sci 4:12. https://doi.org/10.1186/s40645-017-0126-9

Huang P, Sulzbach R, Tanaka Y, Klemann V, Dobslaw H, Martinec Z, Thomas M (2021) Anelasticity and lateral heterogeneities in Earth's upper mantle: impact on surface displacement, self-attraction and loading and ocean dynamics. J Geophys Res Solid Earth. https://doi.org/10.1029/2021JB022332

Martinec Z (2000) Spectral-finite element approach to threedimensional viscoelastic relaxation in a spherical earth. Geophys J Int 142:117–141

Matsuo K, Heki K (2011) Coseismic gravity changes of the 2011 Tohoku-Oki earthquake from satellite gravimetry. Geophys Res Lett 38:L00G12. https://doi.org/10.1029/2011GL049018

Nield GA, King MA, Steffen R, Blank B (2022) A global, spherical finite-element model for post-seismic deformation using Abaqus. Geosci Model Dev 15:2489–2503. https://doi.org/10.5194/gmd-15-2489-2022

Okada Y (1992) Internal deformation due to shear and tensile faults in a half space. Bull Seism Soc Am 82:1018–1040

Pollitz FF (2003) Postseismic relaxation theory on a laterally heterogeneous viscoelastic model. Geophys J Int 155:57–78

Pollitz FF (2020) Coseismic and post-seismic gravity disturbance induced by seismic sources using a 2.5-D spectral element method. Geophys J Int 222:827–844. https://doi.org/10.1093/gji/ggaa151

Sun W (2014) Recent advances of computing coseismic deformations in theory and applications. Earthq Sci 27:217–227. https://doi.org/10.1007/s11589-014-0077-9

Tanaka Y, Hasegawa T, Tsuruoka H, Klemann V, Martinec Z (2014) Spectral-finite element approach to post-seismic relaxation in a spherical compressible Earth: application to gravity changes due to the 2004 Sumatra-Andaman earthquake. Geophys J Int 200:299–321. https://doi.org/10.1093/gji/ggu391

Tanaka Y, Klemann V, Martinec Z (2019) Surface loading of a self-gravitating, laterally heterogeneous elastic sphere: preliminary result for the 2D case. In: Novák P, Crespi M, Sneeuw N, Sansò F (eds) IX Hotine-Marussi symposium on mathematical geodesy. International Association of Geodesy Symposia, vol 151. Springer, Cham. https://doi.org/10.1007/1345_2019_62

Vachon R, Schmidt P, Lund B, Plaza-Faverola A, Patton H, Hubbard A (2022) Glacially induced stress across the Arctic from the Eemian interglacial to the present—implications for faulting and methane seepage. J Geophys Res Solid Earth 127:e2022JB024272. https://doi.org/10.1029/2022JB024272

Whitehouse PL (2018) Glacial isostatic adjustment modelling: historical perspectives, recent advances, and future directions. Earth Surf Dyn 6:401–429

Wouters B, Bonin JA, Chambers DP, Riva REM, Sasgen I, Wahr J (2014) GRACE, time-varying gravity, earth system dynamics and climate change. Rep Prog Phys 77:116801. https://doi.org/10.1088/0034-4885/77/11/116801

Wu P (2004) Using commercial finite element packages for the study of earth deformations, sea levels and the state of stress. Geophys J Int 158:401–408

Zhou J, Pan E, Bevis M (2019) A point dislocation in a layered, transversely isotropic and self-gravitating earth part I: analytical dislocation love numbers. Geophys J Int 217:1681–1705. https://doi.org/10.1093/gji/ggz110